AIMS Materials Science, 3(1): 83-113.
DOI: 10.3934/matersci.2016.1.83
Received: 18 November 2015
Accepted: 11 January 2016
Published: 12 January 2016

http://www.aimspress.com/journal/Materials

Research article

Nacre-like ceramic/polymer laminated composite for use in body-armor applications

Mica Grujicic *, S. Ramaswami, and Jennifer Snipes

Department of Mechanical Engineering, Clemson University, Clemson SC 29634, USA

*** Correspondence:** E-mail: gmica@clemson.edu; Tel: 864-656-5639; Fax: 864-656-4435.

Abstract: Nacre is a biological material constituting the innermost layer of the shells of gastropods and bivalves. It consists of polygonal tablets of aragonite, tessellated to form individual layers and having the adjacent layers as well as the tablets within a layer bonded by a biopolymer. Due to its highly complex hierarchical microstructure, nacre possesses an outstanding combination of mechanical properties, the properties which are far superior to the ones that are predicted using the techniques such as the rule of mixture. In the present work, an attempt is made to model a nacre-like composite armor consisting of boron carbide (B_4C) tablets and polyurea tablet/tablet interfaces. The armor is next investigated with respect to impact by a solid right-circular-cylindrical rigid projectile, using a transient non-linear dynamics finite element analysis. The ballistic-impact response and the penetration resistance of the armor is then compared with that of the B_4C monolithic armor having an identical areal density. Furthermore, the effect of various nacre microstructural features (e.g. surface profiling, micron-scale asperities, mineral bridges between the overlapping tablets lying in adjacent layers, and B_4C nano-crystallinity) on the ballistic-penetration resistance of the composite-armor is investigated in order to identify an optimal nacre-like composite-armor architecture having the largest penetration resistance. The results obtained clearly show that a nacre-like armor possesses a superior penetration resistance relative to its monolithic counterpart, and that the nacre microstructural features considered play a critical role in the armor penetration resistance.

Keywords: personal-protection body-armor; nacre-like composite; computational analysis

1. Introduction

The present work addresses the problem of the use of nacre-like ceramic-reinforcement

polymeric-matrix laminated composites as the so-called trauma plates in personal-protection body-armor applications. Consequently, the concepts most relevant to the present work are: (a) the basics of nacre microstructure and properties; and (b) previous experimental and computational work pertaining to the ballistic-impact performance of nacre-like ceramic-reinforcement polymeric-matrix laminated composites. In the remainder of this section, a brief description is provided for each of these concepts.

1.1. Microstructure and Properties of Nacre

For protection from predators and aggressive-environmental conditions, the shells of bivalve and gastropod mollusks are generally composed of three layers [e.g. 1]: (a) periostracum, the outer layer, consisting of hardened protein; (b) prismatic middle layer, consisting of columnar-grain calcite (a polymorph of $CaCO_3$); and (c) nacre, the inner layer, containing 95% aragonite (another polymorph of $CaCO_3$) and 5% proteins and polysaccharides. The external periostracum layer is hard and brittle and, thus, can provide relatively high initial resistance to impact or another type of external aggression. Nacre, on the other hand, provides high toughness and ductility to the mollusk shell, enabling it to survive external attack without a complete loss of structural integrity. Since the dominant constituent of nacre is aragonite, a relatively hard ceramic material, it is important to understand how the microstructure at all the relevant length-scales of nacre contributes to its ability to undergo (for ceramic materials) unusually high inelastic strains and to its ability to effectively store and dissipate energy.

The complex hierarchical architecture of nacre spans nanometer to millimeter length-scales, as revealed by examining its microstructure. In other words, nacre should be considered as a hierarchical hybrid in which microstructural details at each length-scale and linkages between different length-scales all contribute to the properties of nacre [2].

The following main microstructural length-scales are generally identified in the case of nacre: (a) micron to millimeter lamellar microstructure-scale; (b) micron aragonite-tablet microstructure length-scale; (c) sub-micron mineral bridge scale; (d) nanometer aragonite-tablet grain scale; and (e) sub-nanometer molecular-level scale. Before these microstructural length-scales are described in greater detail, it should be recognized that the main building blocks in nacre are polygonal-footprint thin tablets made mainly of aragonite. The thickness of these tablets is typically in a 0.3–0.5 micron range, with an average in-plane-dimension-to-thickness ratio of 10–20.

1.1.1. Lamellar Microstructure-Scale (Micron to Millimeter)

At this length-scale, the nacre microstructure consists of polygonal (typically six-sided) tablets that are adhesively joined laterally by soft organic materials to form larger-footprint tiles. Then the tiles are arranged in a plane to form even larger-footprint lamellae and stacked (and also adhesively joined by soft organic materials) in the out-of-plane direction. The resulting lamellar microstructure typically possesses one of the following two characteristic architectures [3]:
(a) *columnar*, Figure 1(a).; and (b) *sheet-like*, Figure 1(b).

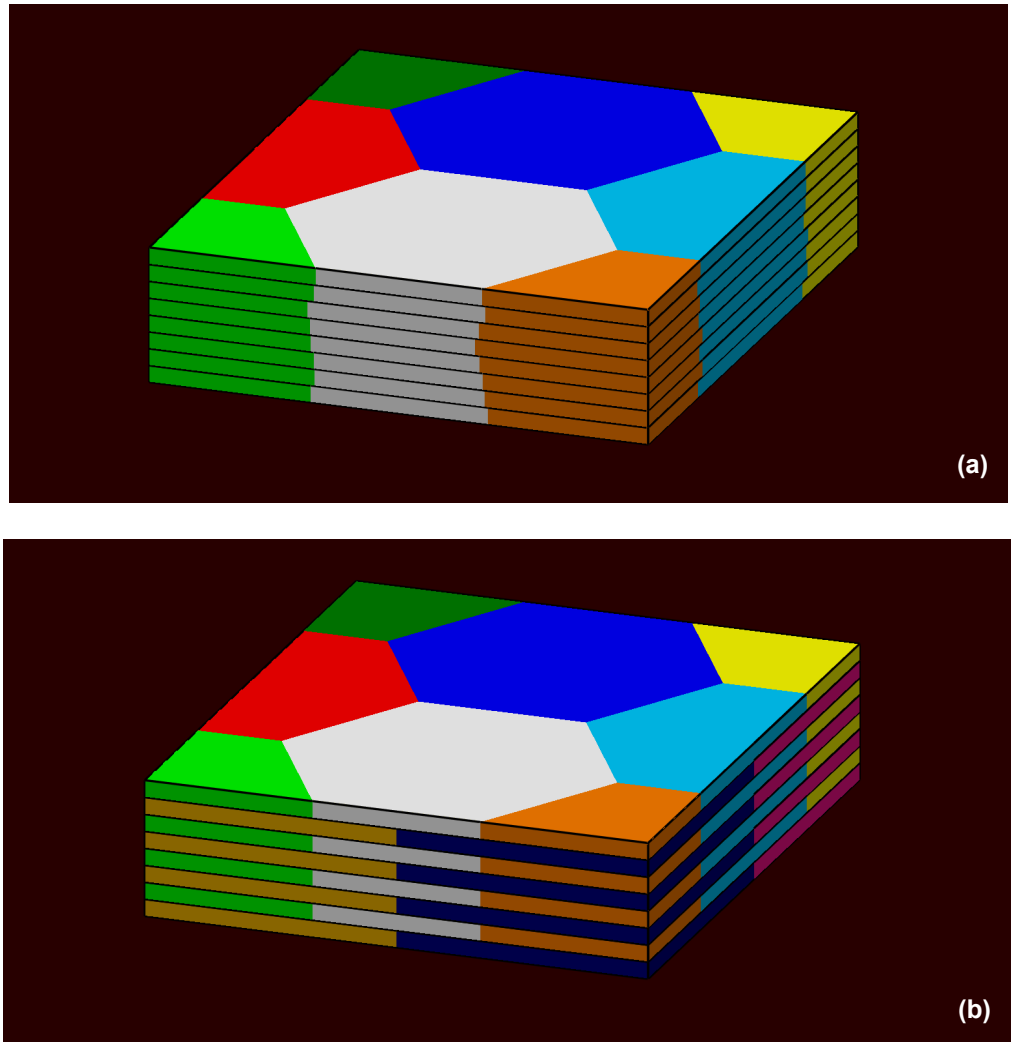

Figure 1. (a) Columnar; and (b) sheet-like lamellar architecture of nacre at the micron-to-millimeter length-scale.

1.1.2. Aragonite-Tablet Microstructure Scale (Micron)

Although aragonite tablets possess a polygonal footprint, they are typically not flat but rather possess a complex surface profile characterized by a greater thickness along the periphery than at the center of the tablet surface. A schematic of a tablet having a hexagonal footprint is shown in Figure 2. Since the contacting tablets of the neighboring lamellae have mating surface profiles, this tablet architecture enables inter-lamellar interlocking during loading [4], which is beneficial from the standpoint of load sharing and energy dissipation.

1.1.3. Mineral Bridge Scale (Sub-micron)

In neighboring lamellae, overlying tablets/tiles are connected by both the soft organic matter and mineral bridges (a few bridges per tablet pair) [5], two of which are shown in Figure 2.

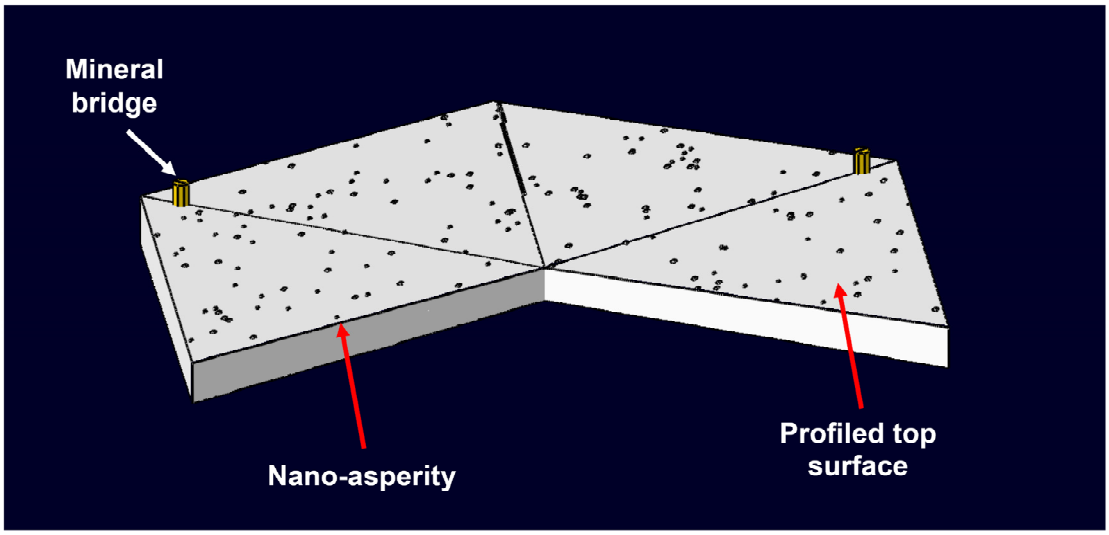

Figure 2. Schematic of nacre tablet with mineral bridges and nano-asperities. A third of the tablet has been removed in order to reveal its surface profiles.

1.1.4. Aragonite-Tablet Grain Scale (Nanometer)

Aragonite tablets are generally polycrystalline, with average grain sizes ranging from 3–10 nm [6]. Furthermore, the individual grains are typically coated with a thin layer of biopolymer which facilitates grain rotation during deformation and increases the fracture toughness and ductility of the material. Aragonite tablets possess surface profiles which enable dovetail-type interlocking between contacting tablets during loading. The tile interlocking is further enhanced by the presence of nanometer-size asperities that increase the effective surface roughness and, thus, the resistance to tile sliding. Nano-asperities are depicted schematically in Figure 2.

1.1.5. Molecular-level Scale (Sub-nanometer)

Nacre consists mainly of aragonite and biopolymer (mainly polysaccharides like chitin and proteins). Thus, at the molecular level the microstructure of nacre depends on the constituent in which the material point is located. When the material point is located in the spaces between the tablets, the molecular structure consists of chitin. Figure 3(a) shows an example of an amorphous unit cell of a chitin-related alpha-D-glucose, $C_6H_{12}O_6$. On the other hand, when the material point is located in aragonite, the material microstructure consists of orthorhombic unit cells of this $CaCO_3$ polymorph. A schematic of the aragonite unit cell is depicted in Figure 3(b).

1.1.6. Mechanical Properties

Efforts have been made to engineer materials with nacre-like microstructure in order to enhance their performance under mechanical loading, because of the superior combination of mechanical properties of nacre. The superior combination of the nacre mechanical properties is clearly related to its hierarchical microstructure, and in the remainder of this section, an attempt is made to identify key microstructural features and key intrinsic processes which make major contributions to the mechanical performance of nacre.

Stiffness and Hardness: Both elastic stiffness [7] and indentation hardness [8] of nacre are relatively high, which could be expected considering their high mineral (i.e. aragonite) content.

Fracture Toughness: On the other hand, the origin of the superior fracture toughness of nacre (higher by two to three orders of magnitude than that of the nacre constituents) is less obvious, considering its high mineral content [9]. Detailed investigation of the mechanical response of nacre has identified a number of potential microstructural features and internal mechanisms which may be responsible for the superior fracture toughness of nacre. The key microstructural features/mechanisms include:

(i) the ability of nacre to "yield" and to undergo (for a ceramic-based material) unusually high inelastic deformation before fracture. The inelastic-deformation process is believed to involve sliding of the contacting tablets of neighboring layers without large-scale degradation of the inter-layer cohesive soft organic material;

(ii) interaction of the nanoscale asperities of the contacting tablets and the associated increase in the sliding friction increases the ability of nacre to spread and dissipate the mechanical energy of deformation; and

(iii) interlocking of the contacting tablets due to their matching surface profiles and the formation of the dovetail-like joints enable nacre to spread the load applied, to one of the tablets/tiles, to a number of surrounding tiles in the lateral and through-the-thickness directions.

Tensile Strength: Considering the fact that the hard reinforcing phase (aragonite) is (effectively) discontinuous, while the soft matrix phase is continuous, it is surprising that nacre retains a major portion of the tensile strength exhibited by aragonite [10]. There are several potential explanations for this finding: (i) the previously mentioned tablet/tablet interlocking along the dovetailed surfaces allows the sliding resistance forces to more effectively oppose the applied tensile loads; and (ii) the mineral bridges between the contacting tablets of the adjacent layers interfere with inter-layer sliding and separation, and thus enhance the delamination resistance of nacre (one of the modes of tensile fracture).

1.2. Prior Relevant Experimental and Computational Work

No experimental study dealing with the ballistic resistance of either natural nacre or nacre-like synthetic materials appears to have been reported in the open-domain literature. This may be the result of the sensitive nature of the subject matter. In general, the experimental work was either concerned with static or low-loading-rate response of nacre-like materials, e.g. Browning et al. [11] or with the measurements of the dynamic properties of nacre-like materials, e.g. Dutta et al. [12].

In their work, Browning et al. [11] investigated the effect of composition (i.e. relative volume fraction of the hard and soft constituents), spatial arrangement (i.e. the degree of hard-phase scale overlap), morphometry (i.e. size and shape of the hard phase) and constituent-material properties (i.e. stiffness, strength, ductility, fracture toughness, etc.) of 3D-printed fish-scale-mimetic armor on its ability to withstand loading by either a blunt or a sharp object. The work focused on identification of the deformation, damage and failure modes within the hard and soft constituents of the armor, and the effect of the aforementioned parameters on the ability of the armor to delocalize loading and damage.

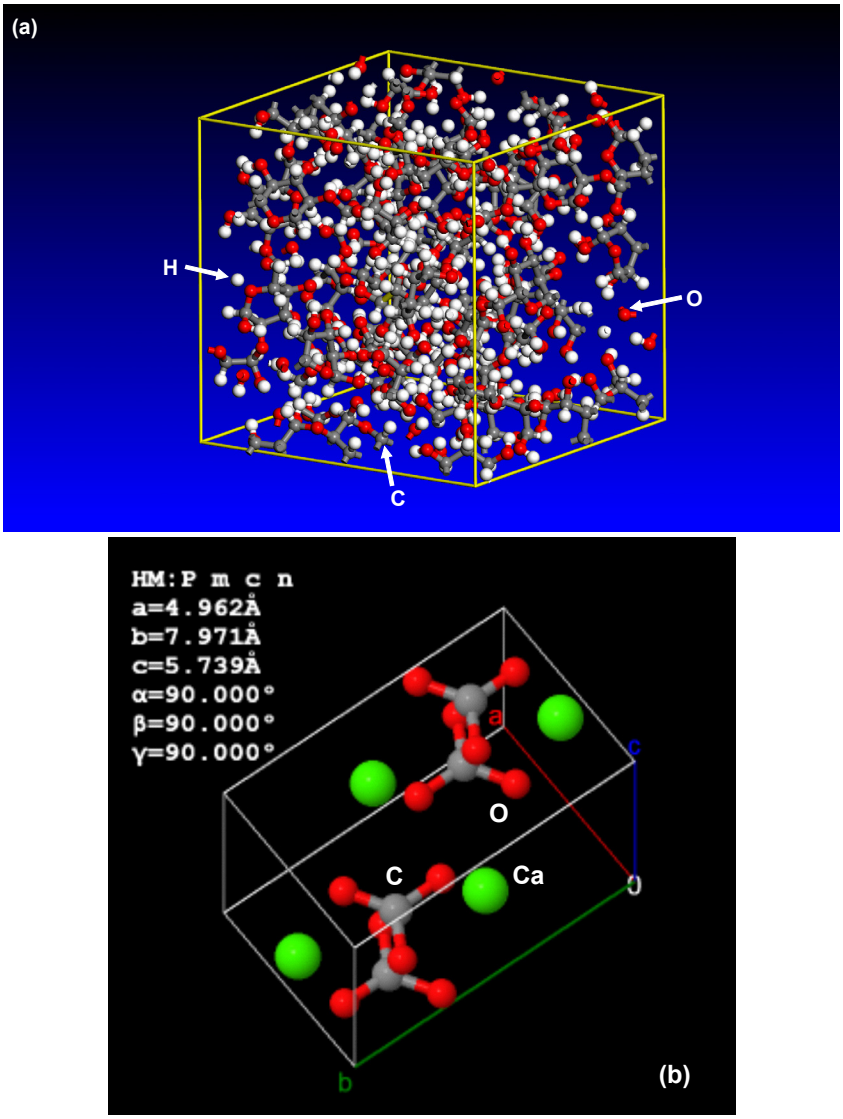

Figure 3. Sub-nanometer microstructure of nacre: (a) the unit cell of chitin-related alpha-*D*-glucose, $C_6H_{12}O_6$ located in the spaces between the tablets; and (b) unit cell of aragonite, a $CaCO_3$ polymorph representing the major constituent of nacre.

An extensive Split Hopkinson Pressure Bar experimental investigation of the dynamic mechanical response of nacre-like composite materials was carried out by Dutta et al. [12]. The composites were fabricated using the so-called freeze-casting method. The results obtained revealed:

(a) an increase in the material compressive strength under dynamic-loading conditions relative to the strength levels observed under static/low-loading-rate conditions. This finding was explained by the viscoelastic nature of the polymeric constituent which stiffens under dynamic-loading conditions and provides a firmer support to the ceramic tables/plates, limiting their extent of bending-induced damage; and

(b) material stiffening under dynamic-loading conditions, which is dominated by the viscoelastic character of the polymer constituent.

While the response of nacre and nacre-like synthetic materials to static and low-loading-rate dynamic loading has been extensively investigated computationally [e.g. 11], there appears to be only one study of a synthetic nacre-like material dealing with its ballistic-penetration resistance [13],

and no such study of nacre. In addition, several papers have been identified, e.g. Tran et al. [14] and Flores-Johnson et al. [15], which deal with the ability of nacre-like armor to mitigate the effects of blast.

In their work, Knipprath et al. [13] employed finite element analysis to simulate the impact of a target-plate made of a synthetic nacre-like composite material by a hard projectile (initially propelled at a velocity of several hundreds of meters per second). The synthetic nacre-like composite material possessed the following features of natural nacre: (a) overlapping tablets of the neighboring layers, as found in bivalves for enhanced damage-delocalization; and (b) tablet-surface profiling to promote tablet/tablet interlocking, for more efficient energy dissipation. The finite-element analysis was next coupled with an optimization algorithm in order to identify an optimal combination of the tile-surface profiling and inter-tile soft-material properties. The results of the combined finite-element/optimization analysis pertaining to the ballistic limit of the nacre-like armor were then compared with their computational counterparts corresponding to the single-block armor made of the same material as the individual tiles in the case of the nacre-like armor. This comparison clearly revealed the advantage offered by the nacre-like armor over the single-block armor, (e.g. the exit velocity of the projectile in the former case was substantially lower) but also exposed some potential limitations (e.g. increased level of high-velocity debris generated at the back-face of the armor). In addition, the benefits offered by the nacre-like armor when used as the backing-plate layer within the multi-layer multi-functional armor were not addressed in the work of Knipprath et al. [13].

Tran et al. [14] simulated underwater blast-loading of a nacre-like armor using finite element analysis. The mechanical response of the armor under blast loading was then compared with that of a conventional composite material made of the same constituents in the same volume fractions as the armor-grade composite, and having the same areal density. The results obtained clearly showed a superior behavior of the nacre-like armor in terms of a lower extent and higher delocalization degree of damage, and a lower magnitude of back-face deflection.

Flores-Johnson et al. [15] showed that as with ceramic-polymer composites, a metal-polymer composite having a nacre-like armor architecture also has improved blast-mitigation capacity. Specifically, under identical blast-loading conditions, the nacre-like armor was found to experience less blast-induced damage, lower particle velocities, as well as reduced maximum back-face deflection relative to their counterparts found in the all-metal single-block armor with the same areal density.

1.3. Main objectives

The main objective of the present work is to assess computationally the suitability of a nacre-like ceramic (B_4C) / polymer (polyurea) laminated composite for use as trauma plates in personal-protection body-armor applications. Towards that end, a finite-element model of a nacre-like ceramic/polymer laminated composite target plate is developed. Then, a transient, nonlinear-dynamics, finite-element analysis is employed in order to investigate the mechanical response (including damage and failure) of such a target plate when subjected to a normal (i.e. zero obliquity angle) impact over a range of incident velocities by a fragment simulating projectile (FSP). To obtain an objective assessment for the suitability of the subject nacre-like ceramic/polymer laminated composite for use as trauma plates in personal-protection body-armor applications, the response of this armor to the ballistic impact is compared with that of a single-block B_4C monolithic-ceramic trauma plate (the nature of the ceramic phase in this case is the same as the hard

phase in the nacre-like composite) with an identical areal density.

2. Problem Definition and Computational Procedure

In this section, the problem related to the normal impact of a series of nacre-like composite target plates by an FSP at different incident velocities (the solid right circular cylindrical geometry of the FSP is generally considered to be representative of a high-velocity fragment) is briefly described. In addition, a brief description is presented of the transient, nonlinear dynamics, finite-element analysis (FEA) used in the computational investigation of this problem.

2.1. Computational model(s)

The basic problem of the computational investigation of a normal (i.e. zero-obliquity angle) impact of an FSP in the shape of a Solid Right Circular Cylinder (SRCC) made of tungsten heavy-alloy, onto a 14-mm-thick nacre-like composite target-plate, is analyzed in the present work. Both the diameter and height of the FSP are 10 mm, and the target-plate consists of 7 equal mean-thickness (ca. 2 mm) B_4C layers (parallel to the x-y plane), with each layer consisting of 20-mm edge-length hexagonal-footprint (complete and partial) tablets. Within each layer, the tablets (complete and partial) are arranged in a regular honeycomb pattern, while tablets in the adjacent layers are displaced in the $-x$ direction by the in-plane tablet edge-length. In most cases, each tablet is assumed not to be flat, but rather to possess a surface profile mirrored across the through-the-thickness midplane of the tablet. The surface profile on each side of the tablet consists of six triangular facets. On a facet of the top surface of the tablet, the vertex having the lowest z-coordinate is associated with the center of the tablet, while the other two vertices of the facet are located along the rim. The z-coordinate of one vertex on the rim remains unchanged during surface profiling, while the other vertex is raised by the amount by which the center point is lowered. To help clarify the geometry of the nacre-like composite target-plate, an exploded view of one half of such a plate is depicted in Figure 4. It is seen that the alternating layers of the target-plate consist of complete and partial hexagonal tablets with an inter-layer shift parallel to the x-axis. It should be noted that since the target plate and the FSP possess a vertical (x-z) plane of symmetry, only one half of the target plate and the projectile needs to be analyzed explicitly. The Cartesian coordinate system employed throughout the analysis is also shown in this figure.

FSP incident velocities in the 300 to 900 m/s range were investigated. While typical FSP incident velocities are substantially higher than the ones investigated here, the effective FSP velocities, once they penetrate the ceramic strike-face and reach the backing plate layer of a multifunctional armor, are in the 300 to 900 m/s range. Since the analysis was confined to the case of normal impact, the angle of incidence was kept constant (90°).

In the present work, an attempt is made to establish whether a nacre-like (B_4C – hard material, polyurea – soft material) composite target-plate provides better ballistic protection, with respect to normal FSP-impact, than a monolithic B_4C target-plate of the same areal density.

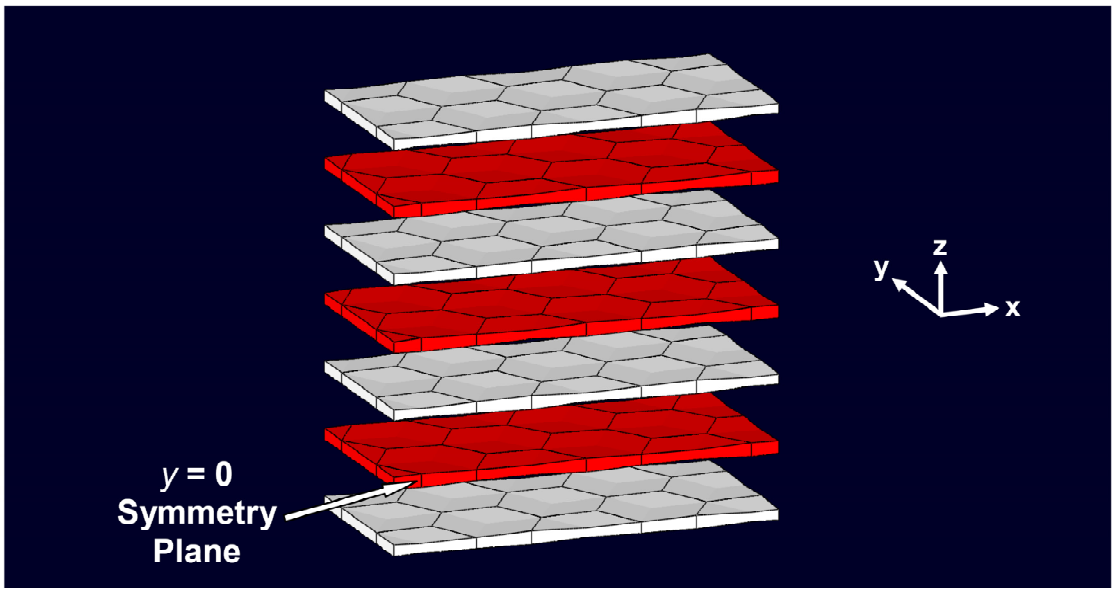

Figure 4. Exploded view of one half of a nacre-like composite target-plate. Surface profiling of the individual tablets is evident, as well as their hexagonal footprint. Adjacent layers are shifted in the *x*-direction by the tablet hexagonal-edge length.

2.2. Finite-Element Analysis

The FEA employed in the present work requires specification of the following: (a) geometrical model; (b) meshed model; (c) computational algorithm; (d) initial conditions; (e) boundary conditions; (f) contact interactions; (g) material models; and (h) computational tool. These aspects are briefly overviewed in the remainder of this sub-section.

2.2.1. Geometrical Model

In addition to the (surface-profiled) hexagonal-footprint B_4C tablets and the FSP described earlier, the geometrical model includes polyurea at the (in-plane and through-the-thickness) interfaces between B_4C-tablets. As will be discussed later, these interfaces are modeled using traction-separation cohesive-zone elements the initial thickness of which was set to zero.

2.2.2. Meshed Model

To address one of the "worst-case scenarios," the FSP was treated as a rigid body, so that no part of its kinetic energy was converted into internal energy through the operation of various deformation, damage and fracture mechanisms. Consequently, the FSP-mesh size was selected in such a way that only the external geometry of the projectile was represented with sufficiently high fidelity, while other aspects of the mesh quality such as the element aspect ratios and element angles were not of concern (due to the rigid character of the FSP). For the one-half of the SRCC-shaped FSP explicitly analyzed, only 16 six-node triangular-prism, first-order solid elements were used with the element height set equal to the projectile length.

The B_4C portion of the target-plate was meshed using six-node, first-order, reduced-integration,

continuum finite elements, with each complete tablet discretized in terms of 2700 such elements, making the total number of B_4C elements (2700 elements/tablet) × (28/3) tablets/layer × 7 layers/plate = 176,400 elements/plate. It should be noted that in the mesh used, the number of elements in the through-the-thickness direction was one. A few calculations were carried out in which the number of elements in the through-the-thickness direction of the tablet was three and five. The key results obtained were found to change, with these two levels of mesh refinement, by less than 1% and 1.05%, respectively. These findings suggested that the use of the meshes containing one element in the through-the-thickness direction of the tablet is adequate and that the additional computational cost (higher by ca. 500% and 900%) was not warranted. To prevent reflection of the stress waves from the circumferential (x_{min} , x_{max} and y_{max}) face/boundary of the target-plate, finite elements adjacent to this boundary were converted into the so-called six-node "infinite" elements. This was done in order to account for the fact that the footprint of the nacre-like composite target-plate investigated is substantially smaller than the surface area of a prototypical body-armor. If the infinite elements were not placed along the circumference of the target-plate, then the impact-induced shockwaves would reflect, as tensile waves, from the lateral faces of the target-plate. Such reflections, however, would not take place (or, more precisely, would take place with a substantial delay) in the case of the body-armor.

The polyurea at the tablet/tablet interfaces was discretized in terms of initial-zero-thickness, eight-node, traction-separation cohesive-zone elements. The traction-separation cohesive-zone elements were a special class of finite elements which enable modeling of the normal- and/or shear-traction-induced interfacial decohesion. Since no B_4C/polyurea decohesion (or shear-fractured polyurea) was present in the initial configuration, these elements were assigned a zero initial thickness. These elements shared nodes with the B_4C solid elements, and hence, their number (154,605: 480 in each odd-numbered layer, 495 in each even-numbered layer, and 25,200 between each pair of adjacent layers) was dependent on the number of elements within the B_4C tablet (2700), the number of tablets within a layer (28/3), and the number of layers within the target-plate (7).

Figure 5 shows a close-up view of the FSP/target-plate meshed model. For clarity, the cohesive elements are not displayed. The location of the cohesive-zone elements is depicted in Figure 6. It is

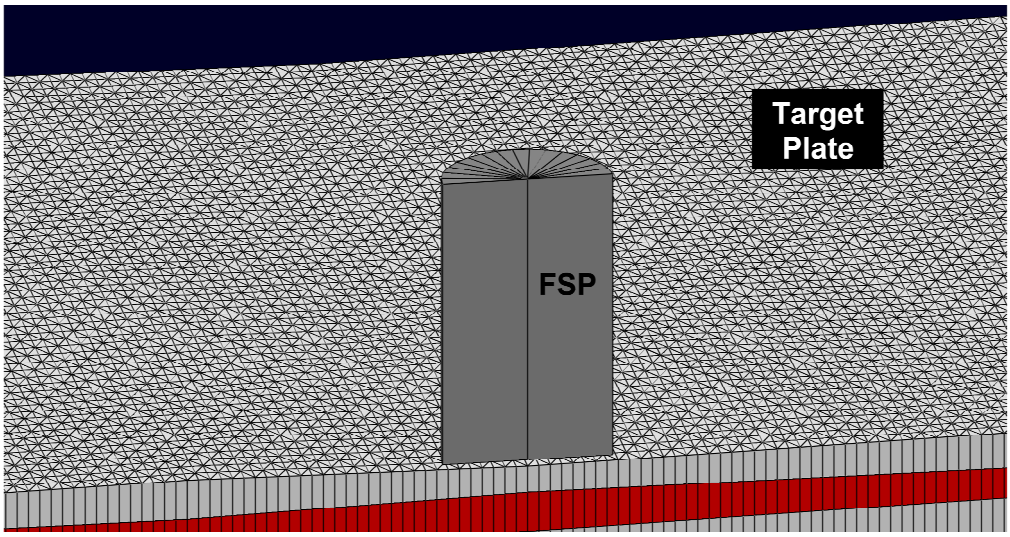

Figure 5. Close-up view of the FSP/target-plate meshed model. For clarity, the cohesive-zone elements are not displayed.

seen that cohesive-zone elements were also used along the symmetry plane at the locations where the symmetry plane coincides with the polyurea interface. In other words, the cohesive elements along the interface were used only at the locations where the symmetry planes pass through the interfaces between tablets, not at the locations where these planes bisect complete or partial tablets.

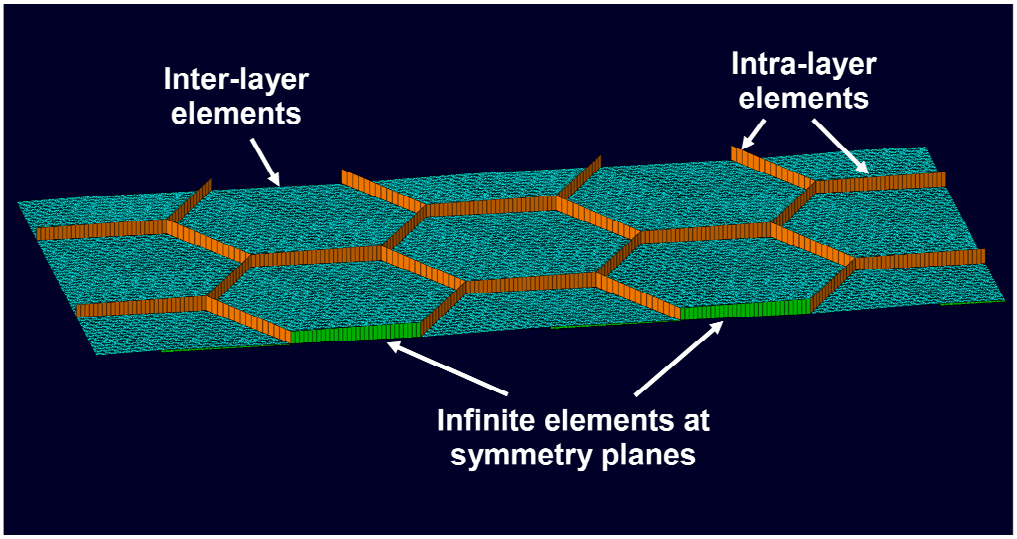

Figure 6. Cohesive-zone elements in the target-plate. Such elements are used within and between layers, and along the symmetry plane at the locations where this plane coincides with the polyurea interface.

2.2.3. Computational Algorithm

A transient, displacement-based, purely-Lagrangian, conditionally-stable, dynamic-explicit finite-element algorithm [16–18] was used for all calculations. Since the FSP/target-plate interactions can result in substantial local-temperature increase and the element dimensions are considerably longer than the FSP/target-plate thermal-diffusion distances, all the calculations were carried out under adiabatic conditions. In other words, FSP kinetic energy dissipation in the form of heat was assumed to increase the temperature only at the location where this dissipation has taken place.

2.2.4. Initial Conditions

Both the FSP and the target-plate were assumed to be stress-free at the beginning of an analysis. In addition, the target-plate was assumed to be stationary/quiescent while the FSP was assigned a normal incident velocity (in the $-z$-direction) in a 300–900 m/s range.

2.2.5. Boundary Conditions

Symmetry boundary conditions were applied over the $y = 0$ plane to comply with the use of a half-model. Specifically, no displacements normal to this plane were allowed. In addition, the bottom

circumferential nodes of the target-plate were prevented from moving in the –*z*-direction (to simulate a rigid back-frame support).

2.2.6. Contact Interactions

The so-called "Hard Contact Pair" type of contact algorithm [19,20] was used to model normal interactions between the FSP and target-plate and their fragments, as well as self-interactions involving the target-plate (and its fragments). Within this algorithm, contact pressures between two bodies are not transmitted unless the nodes on the slave surface contact the master surface. No penetration/overclosure between the slave and master surfaces is allowed, and there is no limit to the magnitude of the contact pressure that could be transmitted when the surfaces are in contact. Transmission of shear stresses across the contact interfaces is assumed to be controlled by a modified Coulomb friction law. This law utilizes a static, μ_{st}, and a kinetic, μ_{kin}, friction coefficient and an upper-bound shear stress limit, τ_{slip} (a maximum value of shear stress which can be transmitted before shearing within the softer material, rather than interfacial sliding, begins to take place).

2.2.7. Material Models

Due to the critical nature of the material models used and a need for a fairly detailed description of these models, such details are deferred to Section 3.

2.2.8. Computational Tool

ABAQUS/Explicit, a general-purpose finite-element program [21], was used to carry out all the calculations in the present work. Within this approach, the problem at hand (formulated in terms of a set of mass, momentum and energy conservation differential equations along with the material constitutive relations, initial, boundary and contact-interaction conditions) is solved numerically using the aforementioned finite-element algorithm. A typical transient non-linear dynamics (half-model) analysis of impact of a FSP onto the nacre-like composite target-plate required 12 hours of (wall-clock) time on a 12-core, 3.0 GHz machine with 12 GB of memory. This (reduced) computational cost was attained after employing variable mass-scaling and viscous-damping algorithms which assist in combating numerical problems associated with highly distorted finite elements and the resolution of the shock waves generated during an impact event.

3. Material Constitutive Models

Based on the geometrical model described, constitutive models are required for: (a) tungsten heavy metal FSP material; (b) B_4C-plate material; and (c) polyurea (Versalink P1000) interface material. In this section, a brief description is provided for the basic features of the material constitutive models in question.

In addition, the ability of the materials to support shock and spreading waves can be properly modeled by separating the total stress tensor into its hydrostatic part (as described by the equation of state) and its deviatoric part (as described by the strength model). Specifically, as discussed in our prior work [22–24]: (a) shock-supporting normal materials must display material non-linearity of a type which yields an upward curvature in the associated pressure vs. specific volume (reciprocal of

the density) plot (i.e., pressure increases at a higher and higher rate as the specific volume decreases); while (b) the anomalous materials must possess a downward curvature in the associated pressure vs. specific volume plot.

3.1. Tungsten Heavy-Alloy Material Model

Since the FSP is modeled as a rigid body, and a dynamic finite-element analysis is employed, the only property for the FSP material, i.e. tungsten heavy-alloy, which needs to be specified is the mass-density, 19,000 kg/m^3.

3.2. B_4C Material Model

The Johnson-Holmquist 2 (JH2) material model [25] is typically employed to describe the mechanical response (including damage and fracture) of technical ceramics such as B_4C under ballistic-impact loading conditions. This type of model is adopted, in the present work, to describe the behavior of B_4C.

The JH2 material model postulates the existence of two terminal material states: (i) an intact material; and (ii) a failed material. The two material states are weighted by a single scalar variable called damage, *D*, the evolution of which is governed by an inelastic (plastic-like) deformation model. The JH2 model also comprises: (a) an equation of state; (b) a strength model; and (c) a failure model.

3.2.1. Equation of State

The JH2 material model describes the hydrostatic response of a material by a polynomial equation of state in which the effect of internal-energy density on pressure is neglected. The pressure vs. degree-of-compression relation in a damage-free material is defined as:

$$P = K_1\mu + K_2\mu^2 + K_3\mu^3, \quad \mu > 0 \quad \text{(hydrostatic compression)} \tag{1}$$

and

$$P = K_1\mu, \quad \mu < 0 \quad \text{(hydrostatic tension)} \tag{2}$$

where degree-of-compression is $\mu = (\rho/\rho_0) - 1$ and ρ is the current density, while ρ_0 (the reference density), K_1 (the bulk modulus), K_2 and K_3 are material-specific constants. After onset of damage in the subject material (i.e. when the extent of damage is no longer zero, $D > 0$), Eq. (2) has to be upgraded to include the effect of bulking. Bulking is a phenomenon associated with the fact that displaced fragments of fractured materials are not generally fully conformable, and consequently, fractured material is associated with a larger volume (a lower density at a constant pressure) than the damage-free material. The bulking-modified polynomial equation of state is then given by:

$$P = K_1\mu + K_2\mu^2 + K_3\mu^3 + \Delta P, \quad \mu > 0 \tag{3}$$

where the bulking-induced pressure increment, ΔP, is determined from energy considerations and varies from zero at $D = 0$ to $\Delta P_{\max}$ at $D = 1.0$. Assuming that a fraction of the internal elastic energy decrease (due to decrease in deviatoric stresses in the material) is converted to an increase in potential internal energy, the bulking-induced pressure increment ΔP at a time $(t + \Delta t)$ can be represented in terms of ΔP at the time t as:

$$\Delta P(t + \Delta t) = -K_1\mu(t + \Delta t) + \sqrt{(K_1\mu(t + \Delta t) + \Delta P(t))^2 + 2\beta K_1 \Delta U} \tag{4}$$

where ΔU is the decrease in deviatoric elastic energy due to damage-induced yield-strength reduction and β is the fraction of the deviatoric elastic energy converted to hydrostatic potential/elastic energy. The decrease in deviatoric elastic energy is given by:

$$\Delta U = U_t - U_{t+\Delta t} \tag{5}$$

where

$$U_t = \frac{\sigma_t^2}{6G} \tag{6}$$

In Eq. (6), σ_t represents the actual compressive yield strength at time t while G, a material parameter, denotes the damage-free shear modulus of the subject material. Eqs. (1)–(6) show that the JH2 parameters: K_1, K_2, K_3, β, and G define the hydrostatic response of the subject material.

3.2.2. Strength Model

The JH2 strength model combines the von Mises yield criterion and normality flow rule with a pressure and strain-rate hardening constitutive relation. The latter is described using a normalized yield strength defined as a damage-weighted rule of mixtures of the corresponding damage-free and fractured yield strengths as:

$$\sigma^* = \sigma_i^* - D(\sigma_i^* - \sigma_d^*) \tag{7}$$

where subscripts ***i*** and ***d*** are used to denote intact and damaged material states and the superscript * indicates that the corresponding yield strength is normalized by the Hugoniot Elastic Limit (HEL) (uniaxial strain) yield strength, i.e.:

$$\sigma^* = \frac{\sigma}{\sigma_{HEL}} \tag{8}$$

The normalized yield strengths σ_i^* and σ_d^* are also defined in the same manner as σ^*. The normalized (pressure- and strain-rate-dependent, ideal-plastic) yield strength of the damage-free material, σ_i^*, and the fractured material, σ_d^*, are respectively given by:

$$\sigma_i^* = A(P^* + T^*)^N (1 + C\ln\dot{\varepsilon}^*) \tag{9}$$

$$\sigma_d^* = B(P^*)^M (1 + C\ln\dot{\varepsilon}^*) \tag{10}$$

where A, B, C, M, N and σ_{HEL} appearing in Eqs. (8)–(10) are all material-specific parameters while P^* and T^* are respectively defined as:

$$P^* = \frac{P}{P_{HEL}} \tag{11}$$

and

$$T^* = \frac{T}{P_{HEL}} \tag{12}$$

where P and T are the actual pressure and the maximum hydrostatic tensile pressure that the subject material can withstand, respectively, and P_{HEL} is the pressure at the Hugoniot Elastic Limit. Finally, the dimensionless material strain rate, $\dot{\varepsilon}^*$, appearing in Eqs. (9) and (10) is defined as:

$$\dot{\varepsilon}^* = \frac{\dot{\varepsilon}}{\dot{\varepsilon}_0} \tag{13}$$

where $\dot{\varepsilon}$ is the actual strain rate and $\dot{\varepsilon}_0$ is the reference strain rate (set in the present work to 1.0 s^{-1}). Eqs. (7)–(13) show that the JH2 parameters: A, σ_{HEL}, P_{HEL}, B, C, M, and N define the deviatoric response of the subject material.

3.2.3. Failure Model

The JH2 failure model defines the evolution/accumulation of damage as:

$$D = \sum \frac{\Delta\varepsilon_p}{\varepsilon_p^f} \tag{14}$$

where $\Delta\varepsilon_p$ is the increment in equivalent inelastic strain with an increment in loading and the failure strain ε_p^f is a pressure-dependent equivalent fracture strain which is defined as:

$$\varepsilon_p^f = D_{1,JH2}(P^* + T^*)^{D_{2,JH2}} \tag{15}$$

where $D_{1,JH2}$ and $D_{2,JH2}$ are material specific parameters.

Within the JH2 failure model, the criterion for fracture is that damage reaches a critical value of 1.0 or negative pressure reaches a value of T. Fractured material has no ability to support any negative pressure, while its ability to support shear is defined by Eq. (10). Eqs. (8)–(15) show that the JH2 failure model parameters: $D_{1,JH2}$ and $D_{2,JH2}$ define the failure response of the subject material.

3.2.4. Parameter Identification

The values of the equation of state, strength and failure material-model parameters identified above, as taken from Ref. [13], are listed in Table 1.

3.3. Polyurea Material Model

3.3.1. Equation of State

The material model reported in Ref. [26] was used to describe the mechanical response of polyurea under high-strain-rate-loading conditions. Within this model, the hydrostatic response of the material is considered to be elastic while provisions are made for large deformations/motions of the material. Consequently, pressure is defined as:

$$P = -K(T)\frac{\ln(J)}{J}; \qquad K(T) = K(T_{ref}) + m(T - T_{ref}) \tag{16}$$

where subscript ref is used to denote a quantity at the reference temperature, K is the bulk modulus, T is the temperature, m a material parameter and $J = \det(\mathbf{F})$, with the deformation gradient $\mathbf{F}$ being a quantity which maps the original/reference material configuration into the current/deformed material configuration and det denoting the determinant operator. Since $\ln(J)$ represents the (logarithmic strain) volumetric strain and J decreases during compression, the effective bulk modulus $\frac{K(T)}{J}$ increases with an increase in volumetric compression. Thus, polyurea also behaves as a normal shock-supporting material. Values of all the parameters for the polyurea equation of state can be found in our prior work [27].

3.3.2. Strength Model

The polyurea material model reported in Ref. [26] assumes the deviatoric response of the material to be time-dependent and treats this response using a geometrically-nonlinear, materially-linear visco-elastic formulation. To account for the aforementioned time-dependent character of the material deviatoric response, the evaluation of the deviatoric stress, σ', at the current time t has to take into consideration the entire deformation history of a given material point from the onset of loading at $t=0$ to the current time. Based on the procedure outlined in Ref. [25], σ' is defined as:

$$\sigma'(t) = 2G_{\infty}\frac{T}{T_{ref}}\int_0^t\left(1+\sum_{i=1}^{n}p_i\exp\left(\frac{-(\xi(t)-\xi(\tau))}{q_i}\right)D'(\tau)\right)d\tau \tag{17}$$

where G_{∞} is the *long-term* shear modulus (i.e., the value of the shear modulus after infinitely long relaxation time), n is the number of terms in the Prony series exponential-type relaxation function, p_i and q_i are respectively the amplitude and the relaxation time of each Prony series term, ξ is the so-called reduced time and D' is the deviatoric part of the rate-of-deformation tensor, D ($D'_{ij} = D_{ij} - (1/3)D_{ii}\delta_{ij}, i,j=1,2,3$, δ_{ij} is the Kronecker delta second order tensor, and summation is carried out over the repeated indices). The reduced time is utilized in order to take into account the effect of temperature and pressure on the relaxation kinetics and is defined as:

$$\xi(t) = \int_0^t \frac{dt}{10^{A(T-C_{TP}P-T_{ref})/(B+T-C_{TP}P-T_{ref})}} \tag{18}$$

where A, B and C_{TP} are material constants. Through application of the reduced-time concept, the response of a material at temperature, T, and pressure, P, over a time period t is assumed to be identical to the response of the same material at the reference temperature and pressure over a time period $\xi(t)$. The rate of deformation tensor, $\mathbf{D}$, is related to the deformation gradient, $\mathbf{F}$, as:

$$\mathbf{D} = sym\left(\dot{\mathbf{F}}\mathbf{F}^{-1}\right) \tag{19}$$

where sym, the raised dot and superscript -1, are used to denote respectively the symmetric part, the time derivative, and the inverse of a second order tensor. Values of all the parameters for the polyurea strength-model can be found in our prior work [27].

Failure Model

A strain-based criterion is defined for failure of polyurea using the following function:

$$\sqrt{\frac{\langle\varepsilon_{ii}\rangle^2}{\varepsilon_{ii,fail}^2}+\frac{\varepsilon_{ij}^2}{\varepsilon_{ij,fail}^2}} \geq 0 \quad i,j=1,2,3 \tag{20}$$

where $\langle ... \rangle$ evaluates to zero when the argument is negative (i.e. compressive strain cannot cause failure of polyurea), summation is implied over repeated indices, and $\varepsilon_{ii,fail}$ and $\varepsilon_{ij,fail}$ are the normal-tensile and shear failure strains.

3.3.3. Cohesive-Zone Material Formulation

Since tablet/tablet polyurea interfaces are not modeled as bulk but rather as traction/separation cohesive-zone interfacial materials, the (bulk) polyurea material constitutive model had to be converted to a cohesive-zone interfacial-material model. Due to space limitations, details of this conversion (similar to the one presented in Refs. [28,29]) will be presented in a future communication. Here, only a brief description of the nature of the resulting cohesive-zone material-model functional relationships is provided. The cohesive-zone material constitutive model includes specification of the (normal and tangential) traction vs. separation functional relationships. These functional relationships are required to account for the following constitutive behavior of polyurea: (a) under compressive normal loading, the magnitude of the normal traction increases (at a progressively higher rate) with an increase in compression; (b) as the stretch increases under tensile normal loading, the normal traction first increases, then reaches a peak and subsequently decreases towards zero (indicating material failure); (c) material behavior under tangential loading is conceptually similar to that under normal loading, i.e. the interfacial material may fail under excessive shear loading; and (d) in the presence of compressive normal loading, shear-induced material failure is delayed/hampered.

The soundness of the formulation of the cohesive-zone interfacial-material model for polyurea, described above, was demonstrated in our prior work [30] by comparing the model predictions with direct experimental measurements. While such a comparison was not drawn here, the same formulation is expected to be applicable, considering the fact that the same grade of polyurea (Versalink P1000) was used in the present investigation.

The cohesive-zone material constitutive relations derived are next incorporated into a *User Element Library* (VUEL) subroutine of ABAQUS/Explicit. The VUEL subroutine allows the user to define the contribution of the cohesive-zone finite elements to the global finite element model. In other words, for the given nodal displacements of the cohesive-zone elements provided to the VUEL by ABAQUS, the contribution of the elements to the global vector of residual forces and to the global Jacobian (element stiffness matrix) is computed in the VUEL subroutine and passed back to ABAQUS/Explicit.

4. Results and Discussion

First, the ballistic performance of the nacre-like composite target-plate (in its reference configuration, defined later) and of a single-block monolithic target-plate with the same areal density are compared. Then the effect of various topological features (e.g. surface profiling, micron-scale roughness, mineral bridges, etc.) on the ballistic performance of the nacre-like composite armor is investigated. It should be noted that, due to space limitations, only the results for one FSP incident velocity (600 m/s) are presented. The remaining results, generated but not shown, while providing some additional information, do not alter the main findings reported in this section.

4.1. Effect of Nacre-like Tessellation and Stacking

The ballistic performance of the nacre-like composite material in its reference configuration and the performance of the single-block monolithic armor made of the same material as the tablets, i.e. B_4C, and having the same areal density, are compared in this section. In the reference configuration, the nacre-like composite material consists of flat (i.e. not surface profiled) tablets and no provisions are made for either surface roughness or mineral bridges. Temporal evolution of the materials during the normal 600 m/s impact by the FSP for the case of the nacre-like composite armor in its reference configuration at the post-impact times of 0.047 ms, 0.094 ms, 0.19 ms, and 0.47 ms is shown in Figures 7(a)–(d). The corresponding results, but for the case of the single-block monolithic B_4C armor with the same areal density as the nacre-like composite armor, are depicted in Figures 8(a)–(d). It should be noted that results like the ones presented in Figures 7(a)–(d) and 8(a)–(d) can be quite beneficial since they may provide an additional insight, not generally attainable through purely experimental means, into the (real-time) temporal evolution and potential interaction between different deformation, damage and failure phenomena and processes. Also, in Figures 7(a)–(d) and 8(a)–(d), as well as in Figures 15(a)–(d), the rigid projectile is not displayed, for clarity, but rather its reference node (labeled as 'X') located at the center of its bottom face, is shown. In these figures, the z translational-velocity component of the FSP is indicated (the x and y translational- and x, y and z rotational-velocity components are set to zero). It should be noted that, for simplicity, the effect of gravity is not considered. An analysis and comparison of the results displayed in Figures 7(a)–(d) and 8(a)–(d) reveals:

(a) While both the nacre-like armor and its single-block monolithic counterpart experience a complete penetration by the FSP, the residual/final velocity of the FSP is substantially lower in the case of nacre-like armor (–31.3 m/s) vs. the monolithic armor (~ –293 m/s), where the negative sign implies that the projectile is moving in the $-z$-direction;

(b) Unfortunately, for both types of armor there is a substantial spallation taking place at the back-face, which produces "high velocity" fragments (moving in the same direction as the incident direction of the FSP). However, the mass and average velocity of these fragments in nacre-like armor are substantially lower than in the monolithic-armor case; and

(c) The superior ballistic-penetration resistance of the nacre-like composite armor (quantified by a lower magnitude of its final/residual velocity) is related to differences in the damage and fracture modes of the two types of armor. That is, in the case of the single-block monolithic armor, the FSP burrows its way into the armor up to approximately half the armor-thickness, then a damage/fracture cone is formed the arrival of which to the armor back-face results in the formation of a large dislodged plug. Since the resistance of the monolithic ceramic to the propagation of the fracture cone is quite low, this type of armor displays a relatively low penetration resistance. It should be recalled that the FSP is modeled as being rigid, so that deformation of the FSP front-end during the burrowing stage is not accounted for. In the case of the nacre-like armor, formation of the damage/fracture cone is not observed and, hence, the FSP has to individually defeat each layer of the armor. In addition, the damage generated within one tablet/layer is arrested at the tablet and interlayer interfaces.

4.2. Effect of Tile-Surface Profiling

The initial results indicated that the nacre-like composite armor, in its reference configuration,

has a stronger ballistic resistance than that observed in the single-block monolithic B_4C armor with an identical areal density. In this section, the effect of tile-surface profiling on the nacre-like composite-armor ballistic performance is investigated. As mentioned earlier, tablets in real nacre are typically not flat but rather possess a complex surface profile. This enables the overlapping tiles to interlock. The results of the investigation carried out in this subsection are summarized in Figure 9, in which the final velocity of the FSP is plotted as a function of the normalized surface-profile amplitude (defined as a ratio of: (i) one half of the difference between the tablet-rim vertex with the largest value of z and the tablet center; to (ii) the tablet half-thickness). Examination of the results depicted in Figure 9 reveals that there is an optimum value of the normalized surface-profile amplitude which yields the maximum value of the (negative) final velocity of the FSP. Careful examination of the results like those displayed in Figures 7(a)–(d) (but not shown for brevity), pertaining to the temporal evolution of the materials as a function of the normalized surface-profile amplitude, reveal that:

(a) at the amplitude values lower than the optimal value, the dovetail-interlocking effect of the overlapping tablets prevails;

(b) while at the amplitude values larger than the optimal one, the tablets, due to their low thickness in the center region, tend to fracture at a higher rate.

4.3. Effect of Tile-Surface Roughness

The results presented in Figure 9 established that the largest ballistic-penetration resistance (as indicated by the smallest residual velocity of the FSP) corresponds to an optimum amplitude of the surface profiling. Also, all the simulations carried out so far involved tablets with smooth facets. In this subsection, the effect of tile-surface roughness on the ballistic performance of the nacre-like composite armor with the optimal level of surface profiling is studied. As mentioned earlier, tablet surfaces in natural nacre are not smooth but rather possess nanometer-size asperities that increase the effective surface roughness and, thus, the resistance to tile sliding (further increasing the degree of inter-tablet interlocking). The results of the investigation carried out in this subsection are summarized in Figure 10, in which the final velocity of the FSP is plotted as a function of the root-mean-square surface roughness (defined as $\left(\frac{1}{N}\sum_{i=1}^{N}\left(Z_i - Z_{smooth}\right)^2\right)^{1/2}$, where Z_i is the height at point i, Z_{smooth} is the height of a smooth surface, and N is the number of points). Examination of the results depicted in Figure 10 reveals that there is an optimum level of surface roughness. Careful examination of the results like those displayed in Figures 7(a)–(d) (but not shown for brevity), pertaining to the temporal evolution of the materials as a function of the surface roughness, reveal that:

(a) at the surface-roughness levels lower than the optimal one, the dominant effect is associated with an increase in the effective shear stiffness and strength of the polyurea interfaces;

(b) while at the surface-roughness levels higher than the optimal one, undesirable surface-roughness-induced stress-concentration effects prevail.

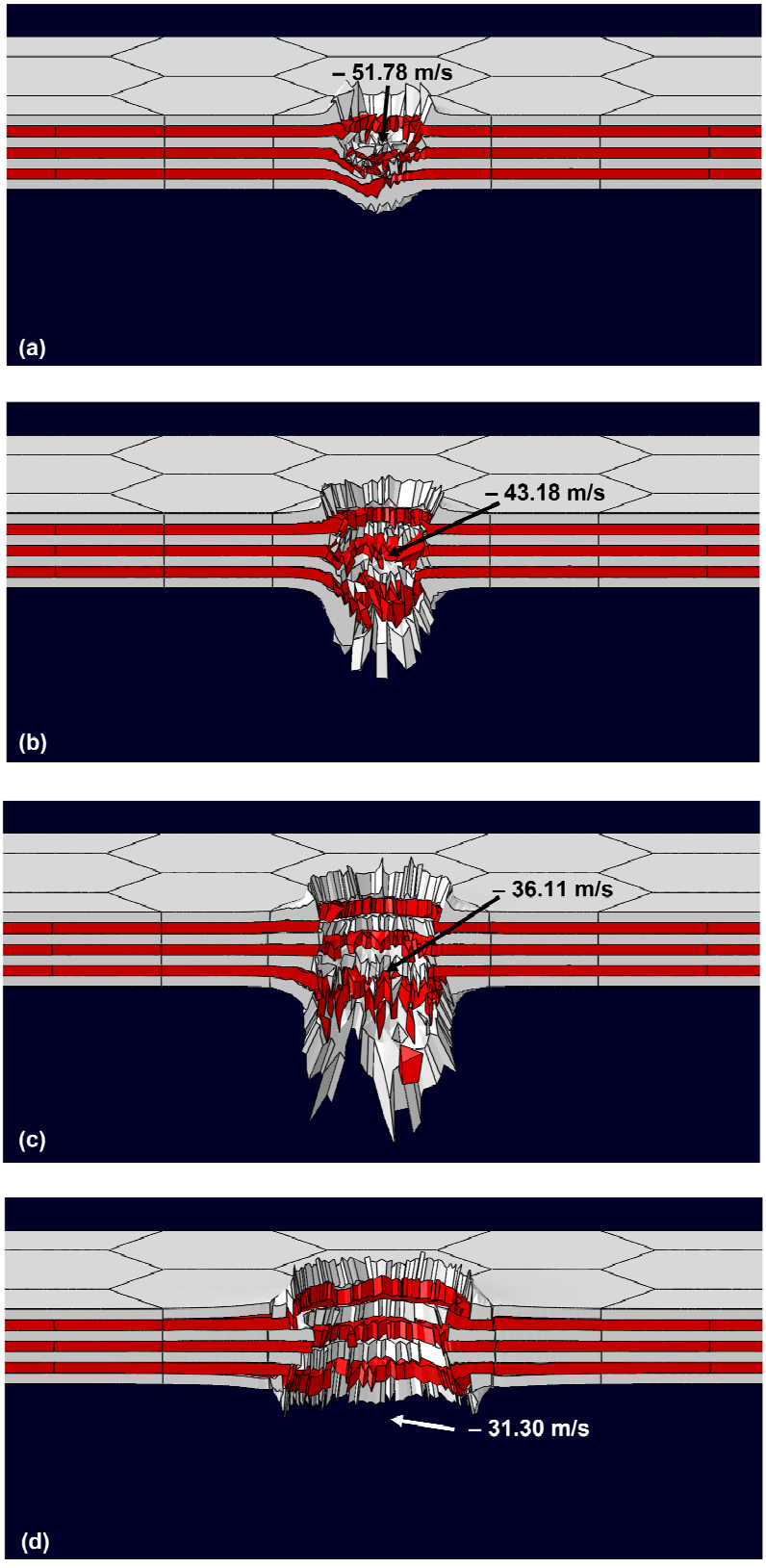

Figure 7. Temporal evolution of the materials during the normal 600 m/s impact by the FSP for the case of the nacre-like composite armor in its reference configuration at the post-impact times of: (a) 0.047 ms; (b) 0.094 ms; (c) 0.19 ms; and (d) 0.47 ms.

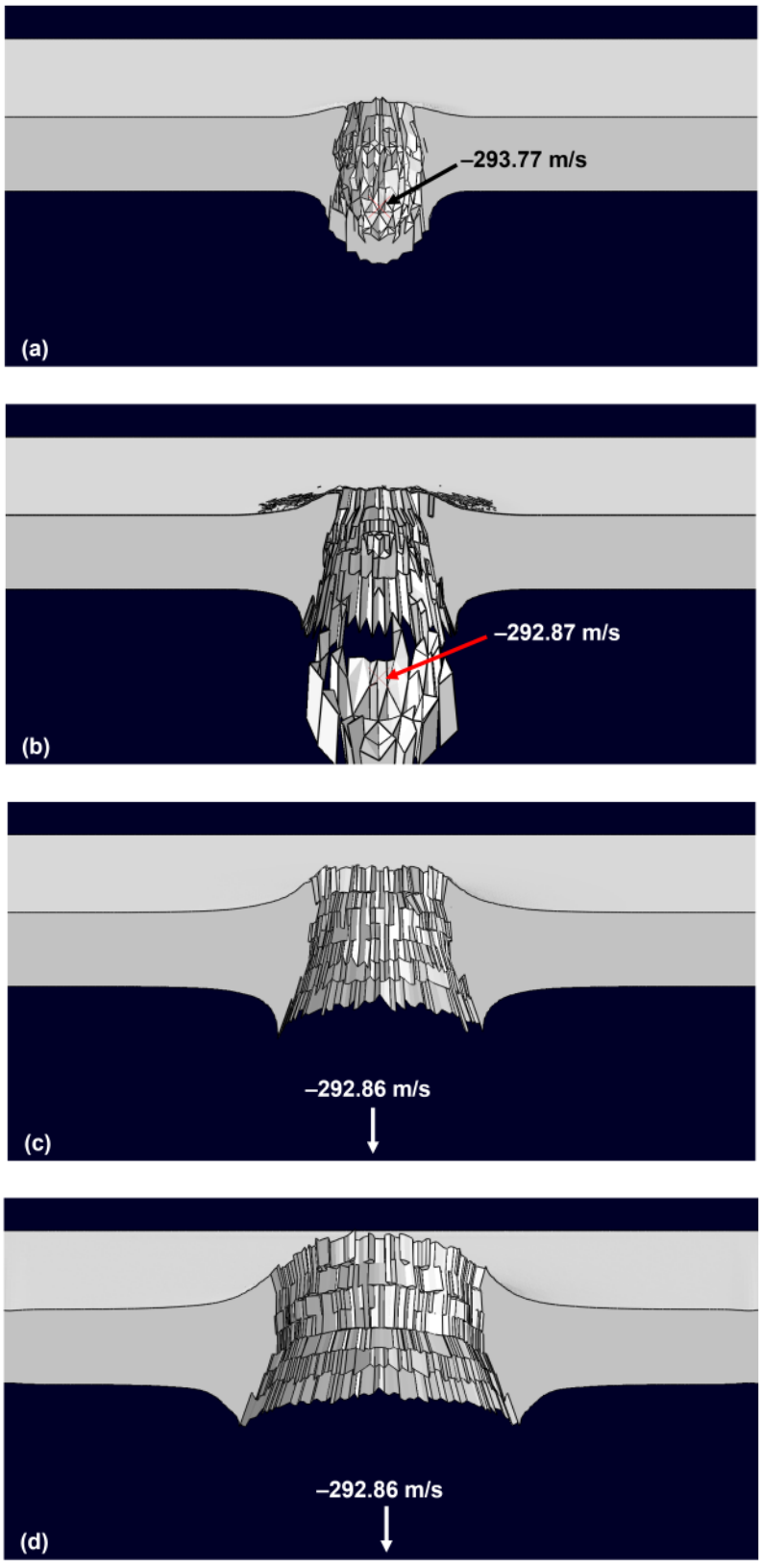

Figure 8. Temporal evolution of the materials during the normal 600 m/s impact by the FSP for the case of the monolithic B4C armor at the post-impact times of: (a) 0.047 ms; (b) 0.094 ms; (c) 0.19 ms; and (d) 0.47 ms.

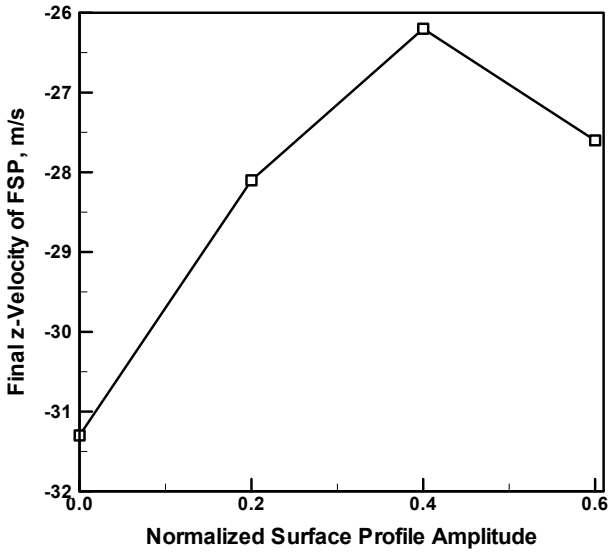

Figure 9. Final velocity of the FSP as a function of the tablet normalized surface-profile amplitude.

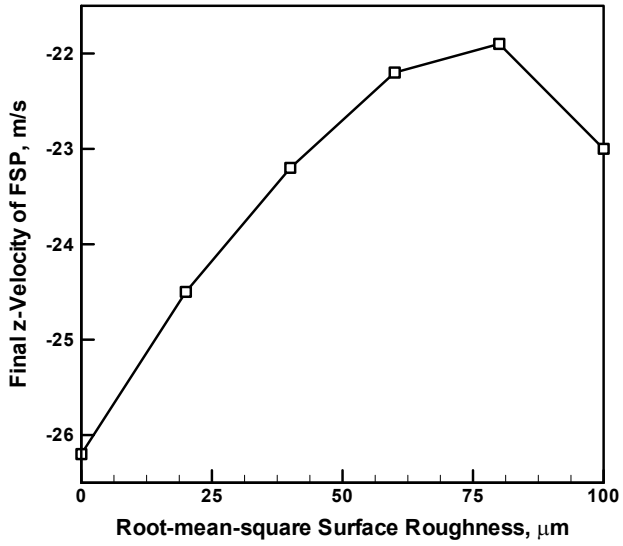

Figure 10. Final velocity of the FSP as a function of the root-mean-square surface roughness.

4.4. Effect of Mineral Bridges

In natural nacre, overlapping tiles residing in adjacent layers are also mutually connected via mineral bridges that play a critical role in the growth of nacre. In this section, the potential role of the mineral bridges in the ballistic-penetration performance of nacre-like composite armor is investigated. Towards that end, two mineral bridges are allocated per tablet, one located on its top face and the other on its bottom face. However, since the nacre-like composite armor analyzed in the present work possesses the previously described "sheet-like" structure, the mineral bridges are not placed in the center of the hexagon. Rather, the top one is located near one of the vertices, so as to connect to the tablet above near the center of that tablet. For the same reason, the mineral bridge on the bottom

of the tablet is located near its center so as to connect to the tablet below near one of the vertices of that tablet. The mineral bridges are modeled as cohesive-zone interfacial materials (like polyurea interfaces) but the constitutive-material properties for it are derived from the B_4C JH2 material model rather than from the polyurea model (details of this derivation will be given in a future communication).

The effect of mineral bridges on the ballistic performance of the nacre-like composite armor with the optimal level of surface profiling and surface roughness is investigated in this subsection. The mineral bridges are assumed to all have a hexagonal cross-section, and to all be of the same size. However, the mineral-bridge edge length is varied between different nacre-like composite-armor architectures. The results of this investigation are summarized in Figure 11, in which the final velocity of the FSP is plotted as a function of the ratio between the mineral-bridge cross-sectional area and the tablet footprint. Examination of the results depicted in Figure 11 reveals that there is an optimum value of the area ratio. That optimal value is associated with the smallest mineral-bridge cross-sectional area which could be obtained for the finite-element mesh used. Careful examination of the results like those displayed in Figures 7(a)–(d) (but not shown for brevity), pertaining to the temporal evolution of the materials as a function of the surface roughness, reveal that for mineral-bridge cross-sectional areas larger than the optimal one, damage/cracking patterns similar to the damage/fracture cone become operational (resulting in a major loss of ballistic-penetration resistance).

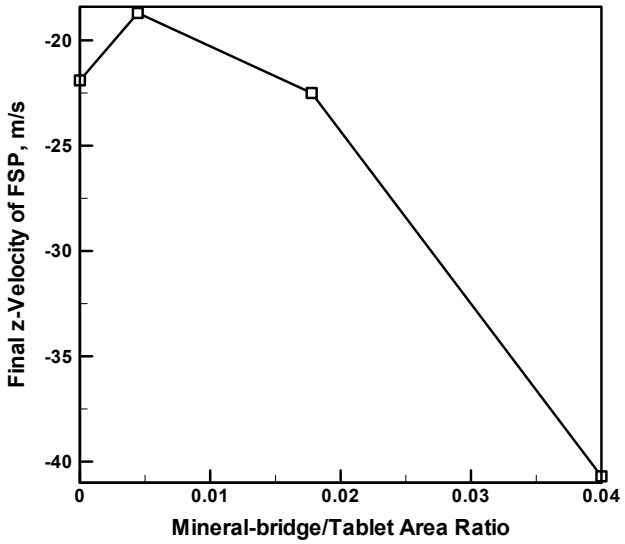

Figure 11. Final velocity of the FSP as a function of the ratio between the mineral-bridge cross-sectional area and the tablet footprint.

4.5. Effect of Nanograin Microstructure

As mentioned earlier, in natural nacre, tablets are made of polycrystalline aragonite with an average grain size in the 3–10 nm range. In addition, individual grains are coated with a thin layer of biopolymer which facilitates grain rotation during deformation and further increases the fracture toughness and ductility of the material. In the present work, the tablets are made of polycrystalline B_4C and neither the effect of nano-crystallinity, nor the effect of grain overcoating by polymer, were

taken into account up to this point. In order to make the composite armor under consideration here be truly nacre-like, these two effects must be taken into account. However, this is a formidable task and had to be undertaken in our separate ongoing effort. The results of this effort will be reported in a future communication. In the remainder of this section, only a few aspects pertaining to, and results obtained in, this effort are reported.

To include the effects of nano-granularity and grain overcoating with polymer on the B_4C-material constitutive response, a procedure involving the following main steps is utilized:

(a) A representative volume element (RVE) is constructed, consisting of several hundreds of equal (10 nm) sized, space-filling, rhombic dodecahedral grains. Each grain has 14 vertices and 12 equal-sized rhombic faces. Within the RVE, individual grains are separated by a 0.1–1 nm thick layer of polyurea;

(b) Following the procedure described in our recent work [31-33], a series of virtual mechanical tests is conducted on the RVE in order to reveal the mechanical response of the material under different loading conditions and, in turn, to derive and parameterize a modified JH2-like material constitutive model for the nano-crystalline and polyurea-augmented B_4C;

(c) The modified material model is then implemented as a material user-subroutine and linked with ABAQUS/Explicit solver;

(d) The implemented new material model is used to describe the constitutive response of the tablet material in the finite element analyses of the FSP normal impact on the nacre-like composite armor; and

(e) An example of the results obtained is depicted in Figure 12, in which the final velocity of the FSP is plotted as a function of the polyurea inter-grain layer thickness. In these analyses, optimal values of the tablet surface-profile amplitude, surface roughness and mineral-bridge cross-sectional area are used. It is seen that substantial additional improvements in the ballistic-penetration resistance of the nacre-like composite material are obtained through the inclusion of the effects of nano-crystallinity and grain overcoating with polyurea. A detailed explanation for this observation will be provided in a future communication.

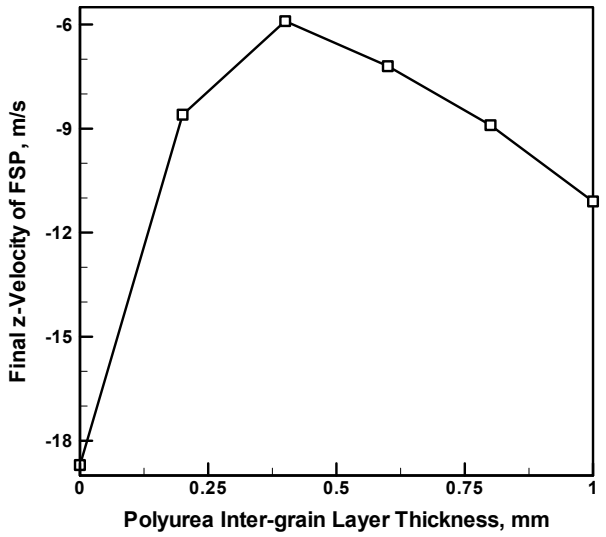

Figure 12. Final velocity of the FSP as a function of the polyurea inter-grain layer thickness.

Temporal evolution of the materials during the normal 600 m/s impact by the FSP for the case of the nacre-like composite armor, with the optimal combination of tablet surface-profile amplitude, surface roughness, mineral-bridge cross-sectional area, and polyurea inter-grain layer thickness (referred to hereafter as the "optimized" nacre-like composite armor) at the post-impact times of 0.047 ms, 0.094 ms, 0.19 ms, and 0.47 ms is shown in Figures 13(a)–(d). Careful examination of the results displayed in these figures clearly reveals the presence of tablet-surface profiling and tablet-surface roughness (mineral bridges could not be seen since they are modeled as cohesive-zone elements). A comparison of the results depicted in Figures 7(a)–(d) and 13(a)–(d) reveals:

(a) The optimized nacre-like armor possesses a higher penetration resistance than the reference nacre-like armor, i.e. the FSP final/residual (still negative) velocity takes on a lower magnitude in the former case;

(b) The extent of spallation at the back-face is comparable in the two renditions of the nacre-like composite armor, and a spall layer in the personal-protection body-armor should be able to contain these fragments; and

(c) Both the overall degree and the spatial dispersion of the damage are somewhat reduced in the case of the optimized nacre-like composite armor. By comparing the results displayed in Figure 13(d) with the corresponding results (not shown for brevity) revealing the effect of surface-profiling, surface roughness and mineral bridges, it is found that nano-crystallinity (including grain overcoating with polyurea) and surface-profiling are the main factors controlling the extent and spatial distribution of the damage.

4.6. Suitability of nacre-like composite material for use in trauma plate soft body-armor applications

Based on the results obtained in the present work, including direct comparison of the optimized nacre-like composite armor results, Figures 13(a)–(d), with the corresponding results for a single-block monolithic B_4C armor, Figures 8(a)–(d), it could be concluded that B_4C + polyurea nacre-like ballistic armor investigated in the present work is a viable personal-protection body-armor trauma-plate material alternative.

4.7. Potential fabrication route for the nacre-like composite material

The results obtained in the present work suggest that the B_4C/polyurea nacre-like composite material exhibits a respectable ballistic-penetration resistance and can be used as a backing-plate layer in a multi-functional armor. In this subsection, a brief description is provided of the main steps involved in one of the possible fabrication routes for such composite materials. The main steps include: (i) Fabrication of B_4C tablets from B_4C flexible green-tape(/foil). The foil is produced using the conventional slip-casting route, which involves: (a) the solution of the selected polymers and auxiliary agents (e.g. liquefiers, binders, plasticizers, dispersing agents and defoaming agents) into solvent (or a mixture of solvents) and the suspension of the B_4C powder to produce castable slip; and (b) the slip is tape-cast and conveyed through a drying furnace to remove the solvent and the auxiliary agents. The resultant foil is highly flexible, with high content of the B_4C powder; (ii) The B_4C foils are cut into 300 mm × 300 mm square laminae; (iii) To create the necessary surface profile for the individual hexagonal B_4C tablets and to enable partitioning of individual tablets within the same lamina, each lamina is stamped/coined between two (3-D printed) metallic dies (with the same footprint as the lamina). In addition, coining produces perforation in the foil around the perimeter of

the individual tablets, which facilitates separation (after sintering, discussed below), by a simple punching action, of individual tablets within the same lamina; (iv) Individually stamped and perforated laminae are coated with a submicron-thick layer of carbon using atmospheric-pressure CVD and methane as a carbon precursor. The presence of the carbon coating is critical for preventing joining of the adjacent laminae during the subsequent sintering process; (v) Individually stamped, perforated and carbon-coated laminae are stacked (while ensuring that the adjacent laminae are in-plane offset in order to enable tablet nesting); (vi) The lamina stack is sintered at 1510 °C for three hours. The first 2.5 hours of the sintering treatment is done under argon atmosphere to ensure that the carbon coating does not oxidize, while the last 30 minutes of the sintering step is done in air to ensure that the carbon layer is completely burned off; (vii) B_4C laminae are next surface-functionalized by placing them in a 1 mM aqueous solution of a pyrogallol derivative for varying amounts of time (to achieve different degrees of functionalization, as characterized using X-ray photoelectron spectroscopy). To remove the solvent, the laminae are dried at 50 °C under vacuum for several hours. Surface functionalization of B_4C tablets is used in order to control B_4C/polyurea adhesion strength; (viii) Next, polyurea is synthesized via a solution route. This is done by dissolving the two polyurea precursors, a diisocyanate and a diamine, in dimethylformamide under vigorous stirring in argon atmosphere; and (ix) The sintered and surface-functionalized lamina stack is next processed using the conventional vacuum-assisted resin transfer molding (VARTM) processing route. Towards that end, starting from the bottom lamina, individual tablets are first punched out and placed into a "rigid" mold. Once the stack of laminae (now consisting of individual hexagonal tablets) is restored, it is encased in a formable vacuum-bag, and impregnated with the polyurea solution by the action of a pressure gradient (induced by a vacuum), gravity and capillary effects. Then the polyurea-solution-impregnated lamina of alumina tablets is heated at 50 °C for 48 hours under vacuum. This ensures the complete removal of the solvent and complete polymerization of polyurea. Upon completion of this step, the as-fabricated nacre-like composite armor is extracted from the vacuum bag.

5. Conclusions

Based on the results obtained in the present work, the following summary remarks and main conclusions can be drawn:

1. The potential of a nacre-like composite material (consisting of B_4C tablets and polyurea interfaces) for use in personal-protection body-armor applications is investigated computationally using a transient, non-linear dynamics finite element analysis of the armor normal-impact by a solid right circular cylindrical rigid projectile.

2. The results obtained clearly reveal that the nacre-like composite material possesses a superior ballistic-penetration resistance relative to that observed in the corresponding single-block monolithic armor having the same areal density and being impacted by the same projectile at the same incident velocity.

3. The effect of various features of the nacre hierarchical microstructure (e.g. surface profiling, micron-scale asperities, mineral bridges between the overlapping tablets lying in adjacent layers, tablet-material nano-crystallinity and B_4C-grain overcoating with polyurea) on the armor-penetration resistance are investigated in order to identify an optimum configuration of the nacre-like composite armor having maximum ballistic-penetration resistance.

4. The results obtained clearly revealed that relative to a reference configuration of the

nacre-like composite armor (having flat, smooth tablets with no mineral bridges nor nano-crystallinity), an optimized configuration of the armor possesses significantly improved ballistic-penetration resistance.

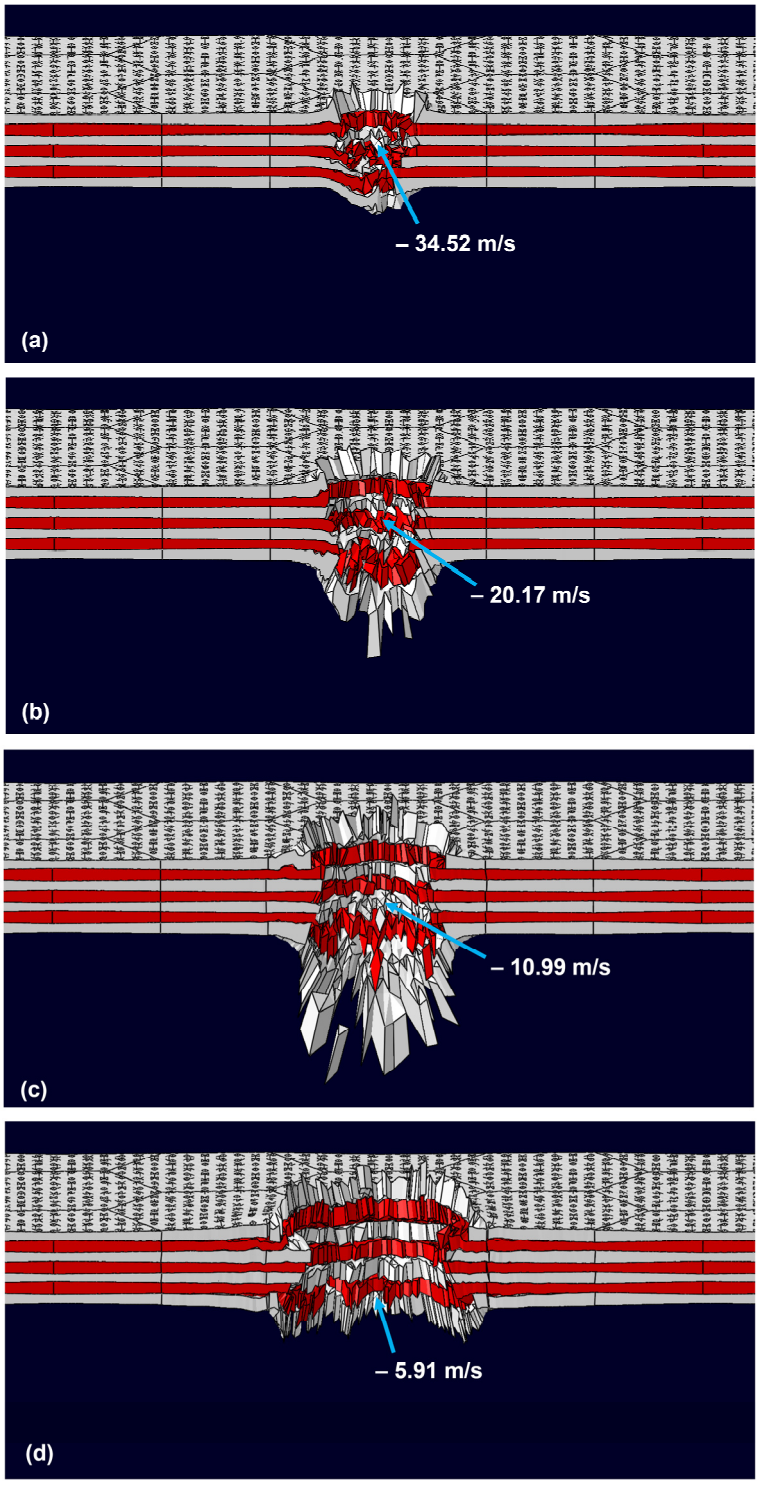

Figure 13. Temporal evolution of the materials during the normal 600 m/s impact by the FSP for the case of the nacre-like composite armor, with the optimal combination of tablet surface-profile amplitude, surface roughness, mineral-bridge cross-sectional area, and polyurea inter-grain layer thickness at the post-impact times of: (a) 0.047 ms; (b) 0.094 ms; (c) 0.19 ms; and (d) 0.47 ms.

5. Since B_4C is a representative technical ceramic and polyurea is a prototypical elastomeric material, the findings yielded by the present investigation are expected to be applicable to a variety of technical-ceramic/-elastomeric nacre-like composite materials.

Acknowledgments

The material presented in this paper is based on work supported by the Office of Naval Research (ONR) research contract entitled "*Reactive-Moiety Functionalization of Polyurea for Increased Shock-Mitigation Performance*," Contract Number N00014-14-1-0286. The authors would like to express their appreciation to Dr. Roshdy Barsoum, ONR, program sponsor, for his continuing support and interest in the present work.

Conflict of Interest

The authors declare that there are no conflicts of interest related to this study.

References

1. Lopes-Lima M, Rocha A, Goncxalves F, et al. (2010) Microstructural characterization of inner shell layers in the freshwater bivalve Anodonta Cygnea. *J Shellfish Res* 29: 969–973.
2. Sun J and Bhushan B (2012) Hierarchical structure and mechanical properties of nacre: a review. *RSC Adv* 2: 7617–7632.
3. Hedegaard C, Wenk H (1998) Microstructure and texture patterns of mollusc shells. *J Mollus Stud* 64: 133–136.
4. Barthelat F, Tang H, Zavattieri PD, et al. (2007) On the mechanics of mother-of-pearl: A key feature in the material hierarchical structure. *J Mech Phys Solids* 55: 306–337.
5. Schäffer TE, Ionescu-Zanetti C, Proksch R, et al. (1997) Does abalone nacre form by heteroepitaxial nucleation or by growth through mineral bridges? *Chem Mater* 9: 1731–1740.
6. Li XD, Chang WC, Chao YJ, et al. (2004) Nanoscale structural and mechanical characterization of a natural nanocomposite material: the shell of red abalone. *Nano Lett* 4: 613–617.
7. Jackson AP, Vincent JFV, Turner RM (1988) The mechanical design of nacre. *P Roy Soc B* 234: 415–440.
8. Mohanty B, Katti KS, Katti DR, et al. (2006) Dynamic nanomechanical response of nacre. *J Mater Res* 21: 2045–2051.
9. Sun JY, Tong J (2007) Fracture toughness properties of three different biomaterials measured by nanoindentation. *J Bionic Eng* 4: 11–17.
10. Currey JD (1977) Mechanical properties of mother of pearl in tension. *P Roy Soc Ser B* 196: 443–463.
11. Browning A, Ortiz C, Boyce MC (2013) Mechanics of composite elasmoid fish scale assemblies and their bioinspired analogues. *J Mech Behav Biomed* 19: 75–86.
12. Dutta A, Vanderklor A, Tekalur SA (2012) High strain rate mechanical behavior of seashell-mimetic composites: Analytical model formulation and validation. *Mech Mater* 55: 102–111.
13. Knipprath C, Bond IP, Trask RS (2012) Biologically inspired crack delocalization in a high strain-rate environment. *J Roy Soc Interf* 9: 665–676.

14. Tran P, Ngo TD, Mendis P (2014) Bioinspired composite structures subjected to underwater impulsive loading. *Comput Mater Sci* 82: 134–139.
15. Flores-Johnson EA, Shen L, Guiamatsia I, et al. (2015) A numerical study of bioinspired nacre-like composite plates under blast loading. *Compos Struct* 126: 329–336.
16. Grujicic M, Pandurangan B, Coutris N (2012) A computational investigation of the multi-hit ballistic-protection performance of laminated transparent armor systems. *J Mater Eng Perform* 21: 837–848.
17. Grujicic M, Bell WC, Pandurangan B, et al. (2012) Effect of the tin- vs. air-side plate-glass orientation on the impact response and penetration resistance of a laminated transparent-armor structure. *J Mater: Des Appl* 226: 119–143.
18. Grujicic M, Snipes JS, Ramaswami S, et al. (2014) Analysis of steel-with-composite material substitution in military-vehicle hull-floors subjected to shallow-buried landmine-detonation loads. *Multidisc Model Mater Struct* 10: 416–448.
19. Grujicic M, Galgalikar R, Ramaswami S, et al. (2014) Finite-element analysis of horizontal-axis wind-turbine gearbox failure via tooth-bending fatigue. *Int J Mater Mech Eng* 3: 6–15.
20. Grujicic M, Ramaswami S, Snipes JS, et al. (2014) Computer-aided engineering analysis of tooth-bending fatigue-based failure in horizontal-axis wind-turbine gearboxes. *Int J Struct Integr* 5: 60–82.
21. ABAQUS Version 6.14, User Documentation, Dassault Systèmes, 2014.
22. Grujicic M, Bell WC, Pandurangan B, et al. (2012) Inclusion of material nonlinearity and inelasticity into a continuum-level material model for soda-lime glass. *Mater Des* 35: 144–155.
23. Grujicic M, Yavari R, Snipes JS, et al. (2014) All-atom molecular-level computational simulations of planar longitudinal shockwave interactions with polyurea, soda-lime glass and polyurea/glass interfaces. *Multidisc Model Mater Struct* 10: 474–510.
24. Grujicic M, Yavari R, Snipes JS, et al. (2014) All-atom molecular-level computational analyses of polyurea/fused-silica interfacial decohesion caused by impinging tensile stress-waves. *Int J Struct Integr* 5: 339–367.
25. Johnson GR, Holmquist TJ (1994) An improved computational constitutive model for brittle materials. In *High-Pressure science and technology, 1993: proceedings of the joint International Association for Research and Advancement of High Pressure Science*, American Institute of Physics, New York, pp. 981–984.
26. Amirkhizi AV, Isaacs J, McGee J, et al. (2006) An experimentally-based viscoelastic constitutive model for polyurea, including pressure and temperature effects. *Phil Mag* 86: 5847–5866.
27. Grujicic M, Bell WC, Pandurangan B, et al. (2010) Blast-wave impact-mitigation capability of polyurea when used as helmet suspension pad material. *Mater Des* 31: 4050–4065.
28. Grujicic M, Chenna V, Galgalikar R, et al. (2014) Wind-turbine gear-box roller-bearing premature-failure caused by grain-boundary hydrogen embrittlement. *J Mater Eng Perform* 23: 3984–4001.
29. Grujicic M, Chenna V, Galgalikar R, et al. (2014) Computational analysis of gear-box roller-bearing white-etch cracking: a multi-physics approach. *Int J Struct Integr* 5: 290–327.
30. Grujicic M, Pandurangan B, d'Entremont BP, et al. (2012) The role of adhesive in the ballistic/structural performance of ceramic/polymer-matrix composite hybrid armor. *Mater Des* 41: 380–393.

31. Grujicic M, Snipes JS, Galgalikar R, et al. (2015). Multi-length-scale derivation of the room-temperature material constitutive model for SiC/SiC ceramic-matrix composites (CMCs). *J Mater: Des Appl* [In press]. DOI: 10.1177/1464420715600002
32. Grujicic M, Snipes JS, Galgalikar R, et al. (2014). Material-Model Based Determination of the Shock-Hugoniot Relations in Nanosegregated Polyurea. *J Mater Eng Perform* 23: 357–371.
33. Grujicic M, Ramaswami S, Snipes JS, et al. (2014). Multi-scale computation-based design of nano-segregated polyurea for maximum shockwave-mitigation performance. *AIMS Mater Sci* 1: 15–27.

AIMS Press